ALUMINUM/ALUMINUM OXIDE STRUCTURED MICROPLASMA DEVICES:
PASCHEN'S LAW AND APPLICATIONS

BY

JEKWON YOON

THESIS

Submitted in partial fulfillment of the requirements
for the degree of Master of Science in Electrical and Computer Engineering
in the Graduate College of the
University of Illinois at Urbana-Champaign, 2010

Urbana, Illinois

Adviser:

Professor J. Gary Eden

ABSTRACT

Aluminum/aluminum oxide microplasma novel devices can be fabricated by sequences of inexpensive wet electrochemical processes and provide an attractive tool to study plasma physics by modifying the device geometry as desired. A wet electrochemical process, used for fabricating microscale cavities and developed at the Laboratory for Optical Physics and Engineering, provides an opportunity to investigate plasma characteristic dimensions decreasing toward ~ 1 µm.

In this thesis, basic background of the plasma physics and experimental techniques necessary for fabricating structured Al/Al_2O_3 devices is presented. In order to better understand and predict device performance as the characteristic dimensions decrease toward ~1 µm, a specific experiment regarding the ignition voltage as a function of various device geometries and gas pressures is performed. The goal of this study is to determine if the fabricated Al/Al_2O_3 devices obey Paschen's Law.

To Father and Mother

ACKNOWLEDGMENTS

First and foremost, I would like to express a gratitude to my adviser, Professor J. Gary Eden, for providing me an opportunity to become a member of the Laboratory for Optical Physics and Engineering. Thanks to his continuous support and guidance, starting from my undergraduate studies, I have gained invaluable experience and knowledge. I also would like to thank Adjunct Associate Professor Sung-Jin Park and Dr. Kwang Soo Kim for their day-and-night training and encouragement. I have benefited from both former and present alumina team members including Jason Readle, Edgar Xie, Andrew Price, Young Seok Kim, Graham Heimberg, Cyrus Rashtchian, Kenechukwu Nsofor, Sung En Kim, Je He Hong, Yeon Joon Moon, and especially Brain P. Chung for his indispensable efforts and time put toward this research. Thank you all. Valuable colleagues in the laboratory including Seung Hoon Sung, Steve S. Lee, In Chan Hwang, Dae-Sung Lee, and especially Taek-Lim Kim always supported me and gave me priceless advice and discussion. In addition, my close friend Hye Sun Park has taught me how to be intuitive and efficiently achieve desired goals during my study. My graduate study here at the University of Illinois at Urbana-Champaign would have not been possible without all these people.

Finally, I would like to express my sincere gratitude to my family members in Korea. Their unconditional faith and trust in me is what fundamentally supported and guided my past ten years of study in the United States. I consider myself very blessed to have such a great family. I will never forget the love I received from them.

TABLE OF CONTENTS

CHAPTER 1

INTRODUCTION

Microplasma is a low temperature, nonequilibrium, and weakly ionized plasma confined to cavities with characteristic dimensions below 1 mm. Such plasmas are of interest because they exhibit characteristics which differ from those of a bulk plasma. Stable glow discharges at atmospheric pressure and above, electron densities up to 10^{16} cm^{-3}, and power loadings ranging from 10^4 to 10^6 $W \cdot cm^{-3}$ can be achieved. This high electron density is attractive in studying plasma frequencies, Debye length, and the behavior of the negative glow; and the opportunity to investigate a previously unexplored region of the plasma space arises as the characteristic dimensions decrease to ~ 5 µm, comparable to the thickness of the sheath region.

Starting from the first successful demonstration of Si-based microplasma devices [1] in the late 1990s, devices fabricated in various material platforms have been developed, and their applications including optical emitters, photodetectors and electron and ion source have been demonstrated [2]. Different platforms studied at the Laboratory for Optical Physics and Engineering include inverted pyramid silicon cavities, ceramics, glass substrates, and aluminum/aluminum oxide (Al_2O_3) structured devices. The first Al/Al_2O_3 structured device was demonstrated in 2005 [3], and has been studied for different purposes including plasma physics, ultraviolet (UV) and vacuum ultraviolet (VUV) radiation applications, and microdischarge thrusters (MCDT) [4]-[11]. Arrays of microcavities in aluminum substrates were, in the beginning, mechanically drilled and had cylindrical geometry. In an effort to improve device performance, an electrochemical cavity etching process has been developed which has resulted

in controlling the vertical cavity wall geometry to a parabolic cross section, and has also presented the opportunity to reduce cavity dimensions to below ~ 50 µm [12]-[14].

Successfully driving microplasma dimensions toward the 1 µm milestone will require an improved understanding of the physics of this unique medium. One tool for probing microplasmas is to investigate their breakdown voltage to determine if Paschen's Law is obeyed.

CHAPTER 2

BACKGROUND

2.1 DC Plasma Discharge

Plasma, the fourth state of matter, can be defined as a collection of charged particles which exhibit quasi-neutrality $n_e \approx N_i^+$ at the macroscopic scale, where n_e is defined as the number density of electrons and N_i^+ represents the number density of ions. Electrons are orders of magnitude lighter than ions and considered to be the dominant species due to their fast speed as compared to ions. The number density of electrons determines the Debye length, λ_D, and the plasma frequency, ω_p, which are expressed by the following relations:

$$\lambda_D = \left(\frac{\varepsilon_0 k_b T_e}{n_e q^2}\right)^{\frac{1}{2}} \tag{2.1}$$

$$\omega_p = \left(\frac{e^2 n_e}{m_e \varepsilon_0}\right)^{\frac{1}{2}}, \tag{2.2}$$

where ε_0 is the permittivity of free space, T_e is the electron temperature in K, and m_e represents the mass of the electron. It should be noted that the Debye length is inversely proportional to the square root of the electron density while the plasma frequency is proportional to the square root of the electron density.

Debye length is the minimum distance required to screen out electric fields in plasmas, and typically the length of a sheath region is considered as being on the order of a few λ_D. Even though quasi-neutrality holds true for the bulk region, this is not the case for the negatively charged cathode region. The sheath region is mostly responsible for accelerating electrons so as to gain sufficient energy for the avalanche process, and therefore is considered one of the most important regions of the plasma. The negatively charged cathode repels incoming electrons

towards the bulk region and the density of electrons becomes much lower than the density of

ions, creating a negative potential which is expressed as:

$$\Phi = \frac{-k_b T_e}{2q} \ln\left(\frac{T_e m_i}{T_i m_e}\right) \ ,$$
(2.3)

where T_i is the temperature of the ions and m_i is the mass of the ions. A qualitative representation

of the key regions near the cathode is shown in Figure 2.1. The sheath region is not electrically

neutral and the current near the cathode is carried primarily by the ions. The ions entering the

sheath region must satisfy the Bohm criterion, and ultimately may yield secondary electrons.
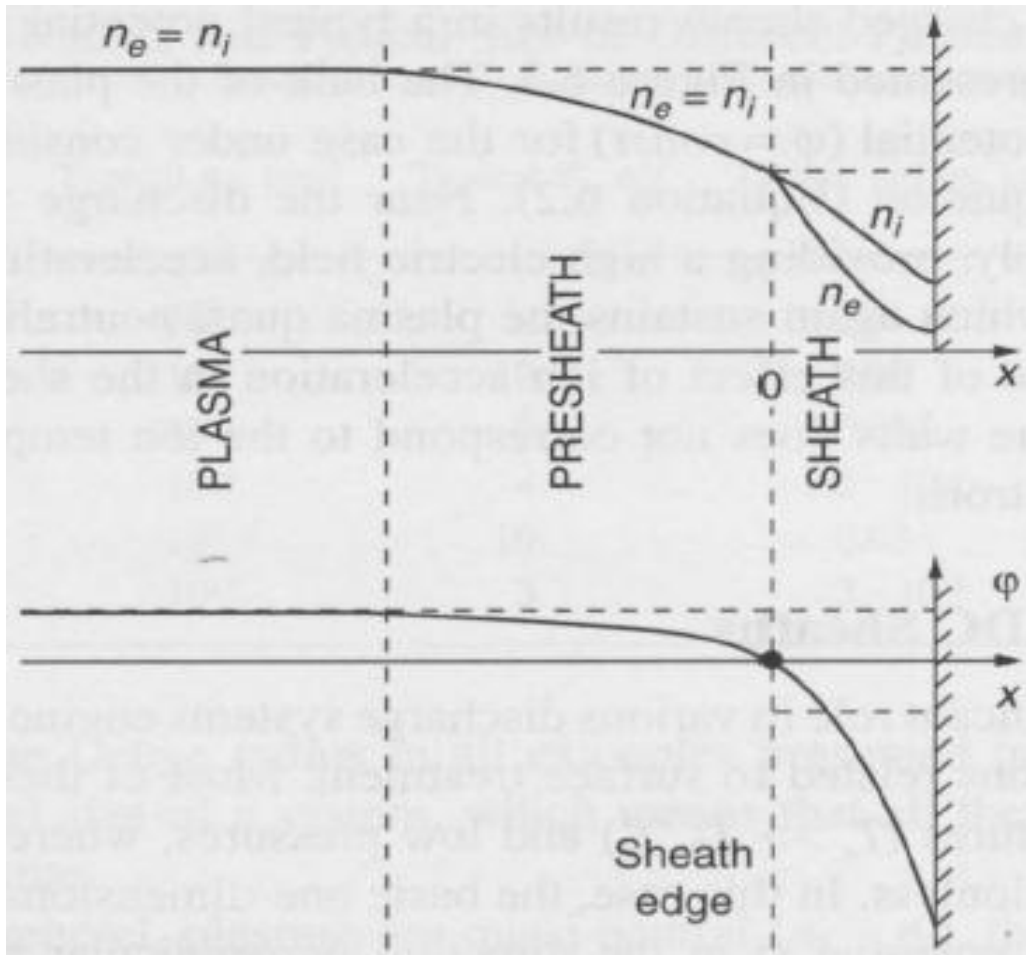

Figure 2.1 Qualitative representations of sheath and presheath behavior near the wall [15].

2.2 Microplasmas

Microplasma, or microcavity plasma, is a low temperature, nonequilibrium, and weakly ionized plasma for which the plasma characteristic dimension is below ~ 1 mm. Some of the plasma characteristics resemble those of a DC plasma, but many unique characteristics are also observed. First, a stable glow mode discharge can be achieved at atmospheric pressure and beyond [9]. This operating pressure differs from many conventional low temperature plasma devices operating at pressures of a few Torr or less. Microplasmas have been found to have electron densities ranging from 10^{13} to 10^{16} cm^{-3} [16], which are orders of magnitude larger than those of conventional low pressure plasma devices such as the fluorescent tube. Because of this high electron density, the Debye length is smaller and plasma frequency is higher than the low pressure plasma devices. Figure 2.2 shows qualitatively the plasma properties that might be able to expect as the characteristic dimensions is varied. As the plasma characteristic dimension falls below 1 mm, the opportunity arises to investigate a previously unexplored region of plasma science.
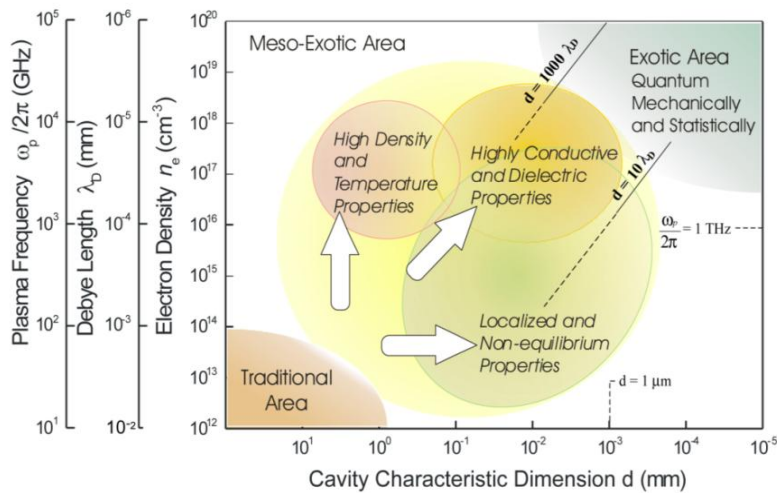

Figure 2.2 Qualitative plasma characteristics as the cavity characteristic dimension decreases below ~ 1 mm [17].

Even though the microplasma device investigated in this dissertation has been excited by a 100 kHz bipolar pulse signal with a duty cycle of 40%, viewing the plasma as a DC system is a valid approximation because of the response time of the electrons when the polarity of electrodes is reversed. For instance, it can be assumed that the averaged drift velocity of the electrons is on the order of ~ $6 \cdot 10^5$ µm/µs from Equation 2.4 with the approximate T_e value of 1 eV. With such speed, the electrons can very easily traverse an electrode gap of hundreds of µm, with a pulse duration of 4 µs, therefore making the DC discharge assumption valid.

$$<v> = (\frac{8kT_e}{\pi m_e})^{\frac{1}{2}}$$ (2.4)

2.3 Paschen's Law

Paschen's law was discovered by Friedrich Paschen in 1889. This law states that the breakdown voltage between parallel plates immersed in gas can be described as a function of the product of the operating pressure, *p*, and the gap between the electrodes, *d*. Paschen's law reflects the Townsend breakdown mechanism and is derived from the discharge current expression:

$$i = \frac{i_0 \cdot \exp{(\alpha d)}}{\{1 - \gamma [\exp{(\alpha d)} - 1]\}}$$ (2.5)

where i_0 is a constant, α is the Townsend's coefficient for ionization, and γ is the secondary emission coefficient which represents the net number of secondary electrons produced per incident positive ion, photon, excited or metastable particle. Gas breakdown is essentially a threshold process and only occurs if the induced electric field exceeds a value characterizing a specific set of conditions [18]. This implies that the gas medium does not ignite while the voltage across a discharge gap is gradually increased and kept under the threshold voltage V_b. Assuming the voltage applied to electrodes is gradually increased from 0 to V_b, so that the state of the gas

medium is unchanged, the discharge current can be understood in light of two different phenomena. With an applied voltage of V << V_b, the induced electric field between the electrodes may enhance the speed of some of the seed electrons, which may result in an electron impact ionization process. The free electron is also accelerated and repeats this process, which can be described as the avalanche process. The avalanche current carried by electrons can be expressed as $i = i_0\exp(\alpha d)$, whereas the current from ions can be expressed as $i_{ion} = i_0[\exp(\alpha d)-1]$. However, as the applied voltage is increased further but kept below V_b, the current saturates as most of the charge particles created in the gas reach the electrodes.

Once the current becomes saturated, then the current becomes dependent on the applied voltage. With a further increase of the voltage to V < V_b, some of the generated ions which satisfy the Bohm criterion may result in the emission of secondary electrons. The secondary electrons generated from a cathode are strongly accelerated in the sheath region and continue the avalanche process, which contributes to creating more charged particles. Since all the secondary electrons travel the full length of the discharge gap, they create more ionization compared to the randomly generated electrons somewhere in the discharge gap.

From the discharge current equation, it is understood that the plasma is ignited when the denominator becomes zero, thereby making the current infinite and self-sustaining. Therefore, the necessary condition $1 = \gamma[\exp(\alpha d)-1]$ is combined with the following expression:

$$\frac{\alpha}{p} = A \cdot \exp(-\frac{B}{E/p}) \tag{2.6}$$

where p is the pressure and the constants A and B are experimentally obtained for different gases. By substituting the electric field with E=V/d and solving for V, the expression for Paschen's law is obtained:

$$V_b = \frac{A(pd)}{\ln(pd)+B} = f(pd) \tag{2.7}$$

7

which is a function of the product of pressure and gap distance. Paschen behavior for various types of gases is presented in Figure 2.3 and the constant values of A and B used for plotting the curves are presented in Table 2.1.

Table 2.1 Experimentally determined constants for the ignition voltage expression [18].

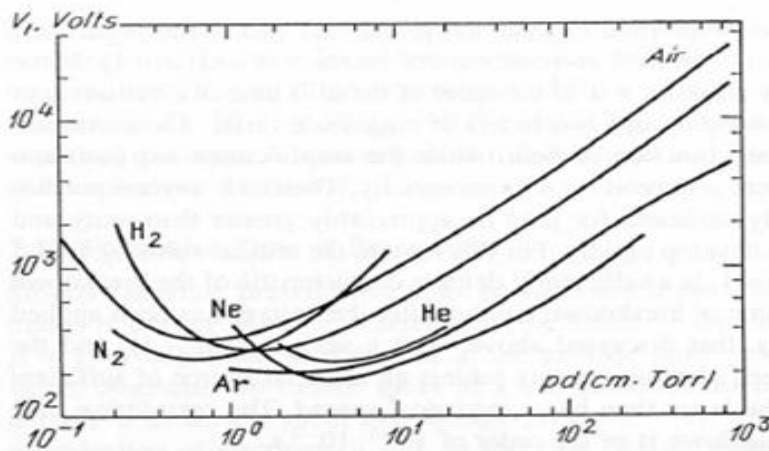| Gas/Constants	A (cm^{-1}Torr^{-1})	B (V·torr^{-1}cm^{-1})
He	3	34
Ne	4	100
Ar	12	180
Kr	17	240
Xe	26	350
Hg	20	370
H_2	5	130
N_2	12	342
N_2	8.8	275
Air	15	365
CO_2	20	466
H_2O	13	290

Figure 2.3 Breakdown potentials in various gases over a wide range of pd values from 10^{-1} to 10^3 Torr·cm on the basis of data given in Table 2.1 [18].

It should be noted that this law is originally derived from a parallel plate DC discharge device with a homogeneous electric field, and may be applied differently depending on the device geometry. In the case of microhollow cathode devices with the structure shown in Figure

2.4, it has been found that the effective distance for Paschen's law is the cavity diameter, D, instead of the anode-cathode distance d [8].
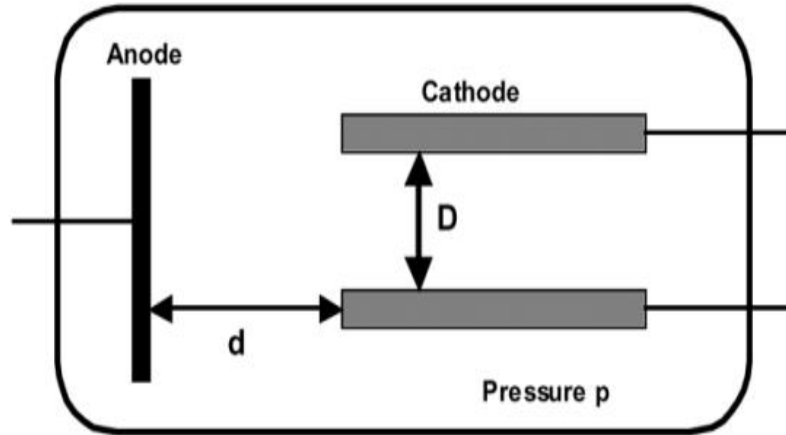

Figure 2.4 General diagram of hollow cathode discharge device [19].

Device structures developed in the Laboratory for Optical Physics and Engineering in the past few years depart from both parallel plates and microhollow cathode devices, and have unique structures which are now under study. Cavity dimensions are less than ~200 μm, and typically one cavity is placed on top of another cavity as shown in Figure 2.5. For this structure, the top cavity diameter is varied from 50 μm to 200 μm and the bottom cavity diameter ranges from 0 μm (planar foil) to 200 μm. The foil thickness is varied from 30 μm to 130 μm.
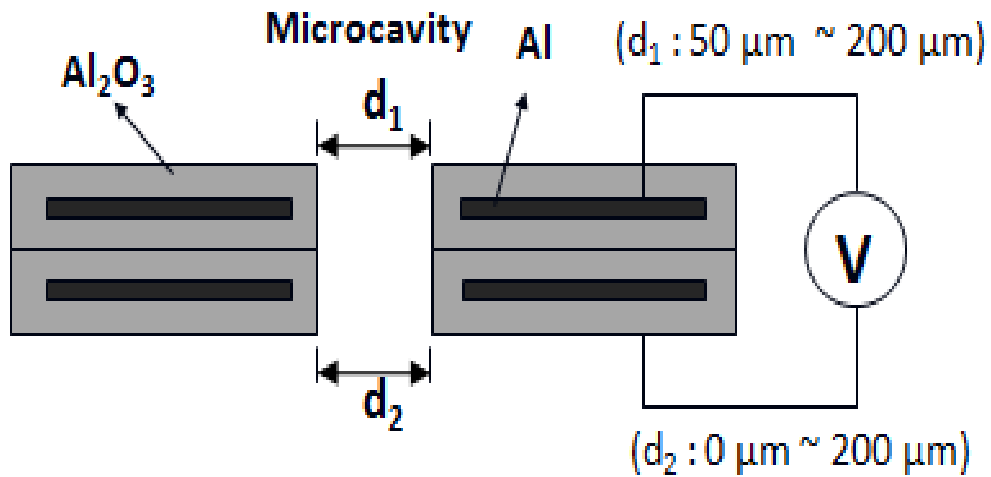

Figure 2.5 Generalized cross-sectional schematic of an Al/Al$_2$O$_3$ microcavity device.

In order to better understand the behavior of microcavity devices developed at the University of Illinois, experiments determining the device breakdown voltage on devices with cavity dimensions of less than 225 µm are performed, with the aid of geometry controlling techniques developed by the members of the laboratory with operating pressure of 400 Torr to 1100 Torr. The history of the development of these techniques is described in Chapter 3.

CHAPTER 3

EXPERIMENTAL TECHNIQUES

In this chapter, the two most important experimental techniques required to fabricate Al/Al_2O_3 devices for studying Paschen's law are presented. The growth of anodic aluminum oxide and electrochemical etching of aluminum are essential since they provide a convenient and powerful tool to precisely control the device sidewall geometries with the precision of ± 2 %. The details of the two techniques are described.

3.1 Anodic Aluminum Oxide

Anodic aluminum oxide consists of two different types of layers [20] as shown in Figure 3.1, and the key mechanism of the growth process has already been explained in detail [21]-[24]. Due to the highly ordered porous structure of aluminum oxide, applications such as the synthesis of nanowires, and carbon nanotubes with controllable height and aspect ratio, have received significant attention [25]-[27]. This structure also is attractive in studying two-dimensional photonic crystals due to its periodic pores of small diameter ranging from tens to hundreds of nanometers.
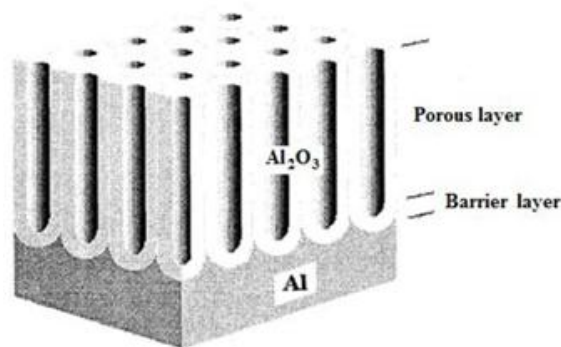

Figure 3.1 Schematic diagram of a porous aluminum oxide [28].

This periodic porous structure also is known to have superior dielectric properties compared to bulk aluminum oxide. For instance, a 20 µm thick nanoporous Al_2O_3 film is measured to exhibit a breakdown voltage of 2000 V which is >60% larger than the breakdown voltage of a 40 µm wafer of bulk Al_2O_3 [29]. From the point of view of an operating dielectric barrier discharge (DBD) device, this higher breakdown strength is considered to be significant.

Nanoporous Al_2O_3 is grown onto an aluminum substrate by an inexpensive wet chemical process. Graphite or copper plate is used as a counter electrode with the aluminum substrate as an anode. The electrodes are then placed in an isothermal bath filled with 15 °C 0.3 M oxalic acid and a voltage of < 50 V is applied to the electrodes to grow the structured Al_2O_3. An example of the resulting structured Al_2O_3 film is presented in Figure 3.2.
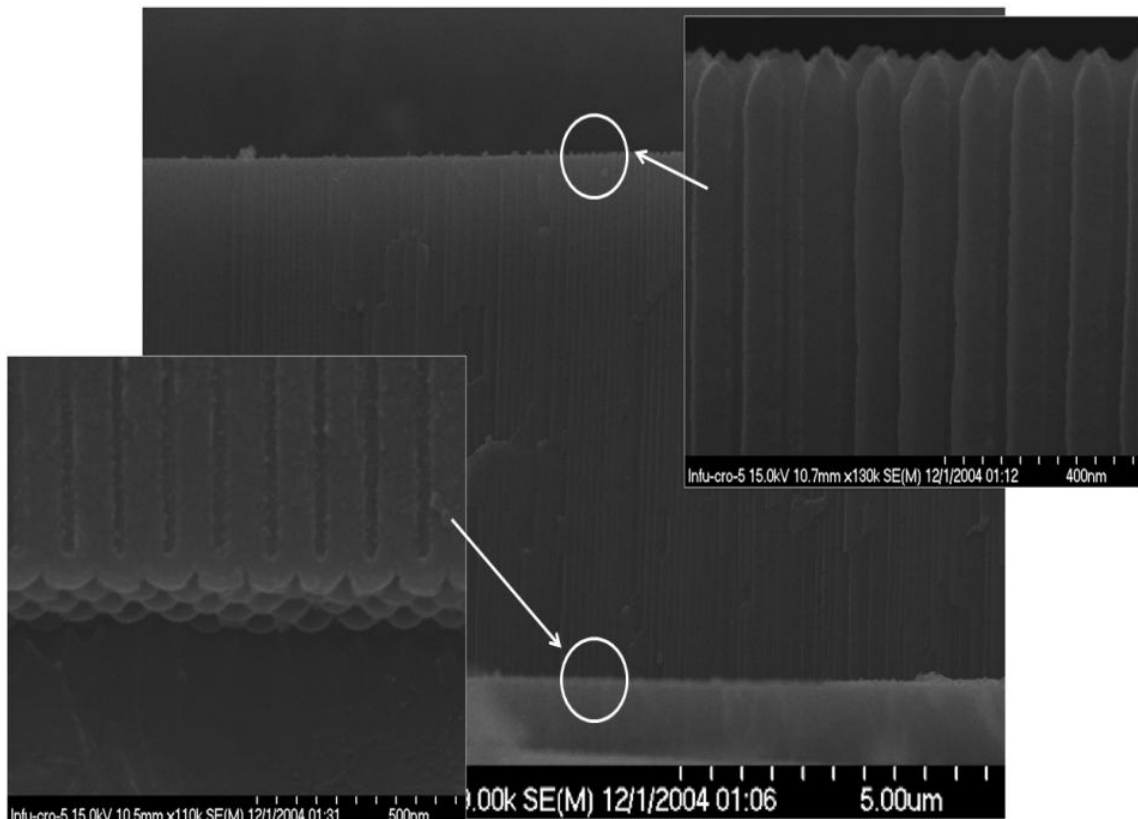

Figure 3.2 Cross-sectional SEM image of porous Al_2O_3 layer on aluminum substrate interface. Different regions are magnified to illustrate details of the film [30].

Typically, film thicknesses of 5 ~ 40 µm are grown on aluminum and the growth rate has been measured to be ~5 µm/h. Since this Al_2O_3 growth process is a wet process, various different form factors can be conveniently achieved.

The porous Al_2O_3, encapsulated on an aluminum substrate is then used to fabricate Al/Al_2O_3 structured microplasma devices. First, aluminum foil is mechanically drilled, and the drilled aluminum is then wet chemically anodized at 30 V with 15 °C of 0.3 M oxalic acid for 6 h. The resulting Al_2O_3 device is shown in Figure 3.3.

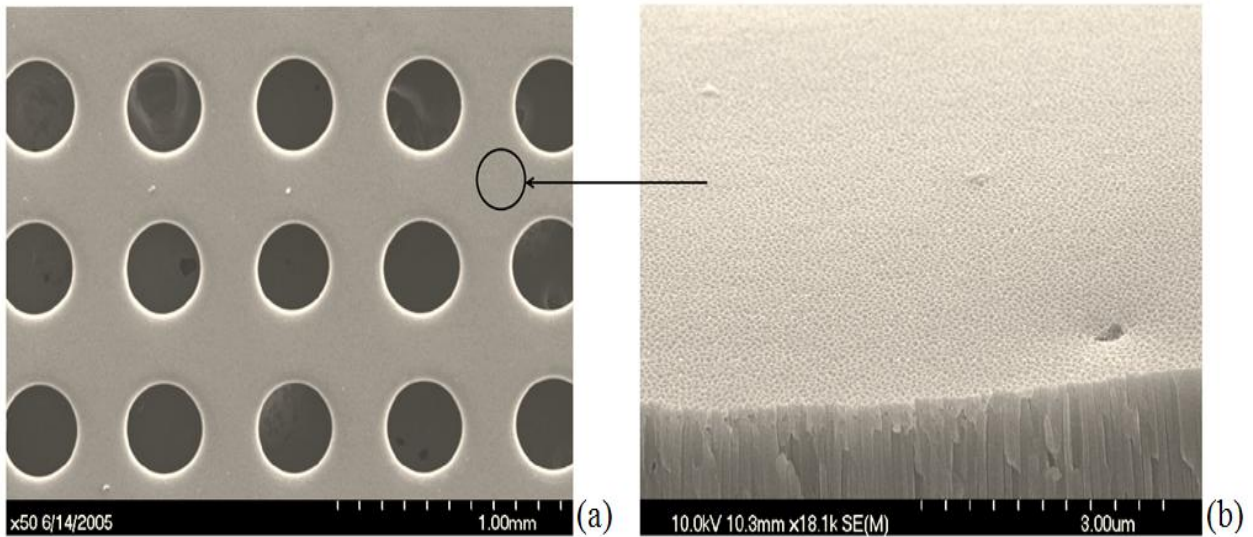Figure 3.3 (a) SEM image of a segment of an array of Al/Al_2O_3 devices. Each cavity has a diameter of 300 µm. (b) SEM of a portion of the Al_2O_3 film surface.

Fabricated devices with the sequences of wet processes were operated in various rare gases and mixtures of gases such as Ne, Ar, Ne/Ar, Ne/Xe, and Ar/N_2, and emission wavelengths ranged from the VUV to the visible. For these experiments, the driving voltage of 5~20 kHz is sinusoidal with operating pressures ranging from 400 Torr to atmospheric pressure.

3.2 Electrochemical Aluminum Etching

3.2.1 Formation of microcavity

The mechanical drilling method is limited when reducing the cavity size below ~50 µm due to the mechanical strength of the small drill bits. It is also practically limited when the number of the cavities in an array increases over ~50. In order to overcome such constraints, a method other than mechanical drilling has been developed in our laboratory. This is done by a wet electrochemical method that is proven to solve the problems associated with mechanical drilling. The generalized process is presented here, but it should be noted that some of the processing conditions may be varied when different cavity geometries such as smaller size or different shape are desired.

First, the entire aluminum substrate is anodized in 15 ℃ of 0.3 M oxalic acid at 40 V for 0.5 h. Then a 50 x 50 µm square opening window is patterned by photolithography with AZ4620 positive resist, and the exposed Al_2O_3 layer is chemically etched away in mixtures of chromic acid and phosphoric acid at 50 ℃ for 0.5 h. Once the 50 µm^2 Al_2O_3 layer is selectively removed, thereby exposing aluminum to the etchant, the electrochemical etching of aluminum is performed in mixtures of perchloric acid and ethyl alcohol at 0 ℃ with an applied DC voltage of 30 V. The aluminum etching duration is plotted as a function of aluminum foil thickness. In Figure 3.4, the aluminum etching rate is measured to be less than ~ 1.5 µm/min.

The resulting cavity diameters are dependent on the aluminum etching duration, which influences the undercutting of the aluminum. For instance, a 50 µm^2 opening with a foil thickness of 60 µm (±2 µm) and etching duration of 70 min results in ~150 µm diameter cavities. Microphotographs of cavities fabricated on foils of different thicknesses are presented in Figure

3.5. The smallest cavity fabricated to date is 45 µm in diameter on an aluminum foil with a thickness of 40 µm and an opening mask size of 30 x 30 µm.
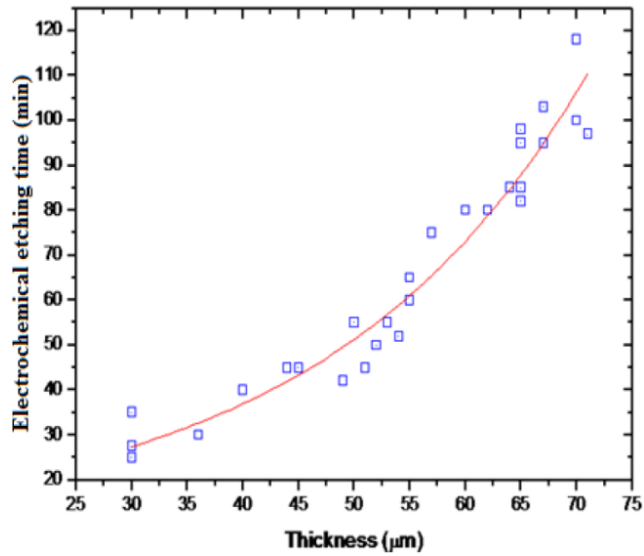

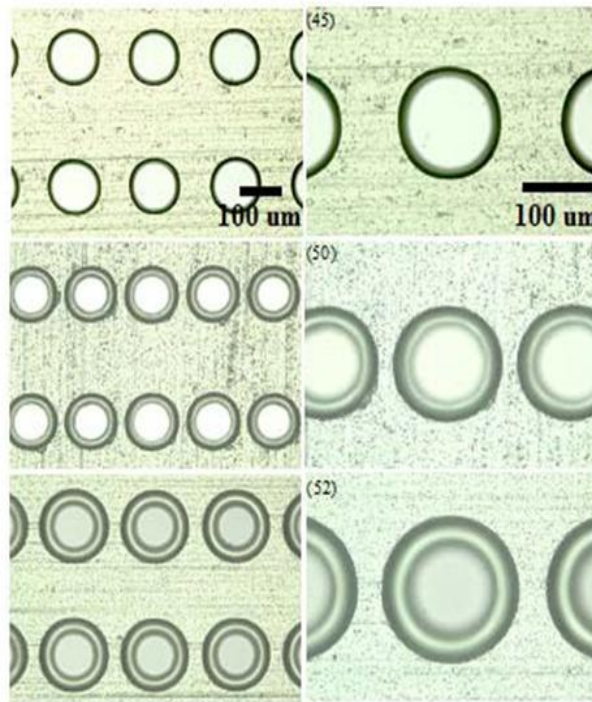Figure 3.4 Microcavity etching duration as a function of foil thickness.

Figure 3.5 Optical micrographs of microcavity arrays fabricated by an electrochemical etching process with foil thicknesses of 45, 50, and 52 µm.

3.2.2 Microcavity geometry control

The sequence of wet electrochemical processes which result in creating a parabolic cross-sectional microcavity is influenced by many parameters such as the dimensions of the square opening window, the aluminum foil thickness, stirring rate of the etchant, and the aluminum etching duration. The resulting parabolic sidewall contour is caused by the isotropic property of the wet electrochemical etching process. Also, the wall geometry can be made linear if the refreshment of etchant is limited. In our experiment, the refreshment is limited by reducing the opening window dimensions below 50 µm, adjusting the foil thickness, and increasing the etching duration for deeper undercutting. The experimentally measured wall geometry curves as a function of etching duration with foil thickness fixed at 55 µm are presented in Figure 3.6. As shown in the figure, the sidewall of the cavity contour changes as the etching duration increases from 60 to 120 min. As the etching duration increases, the lateral etching increases and the refreshment becomes harder, disturbing the isotropic property of the process.

$$(Vertical \quad Scale) = \sqrt{(9.276 \times 10^{-6} \cdot Etching \quad Time - 3.464 \times 10^{-4}) \cdot (Horizontal \quad Scale)^2}$$
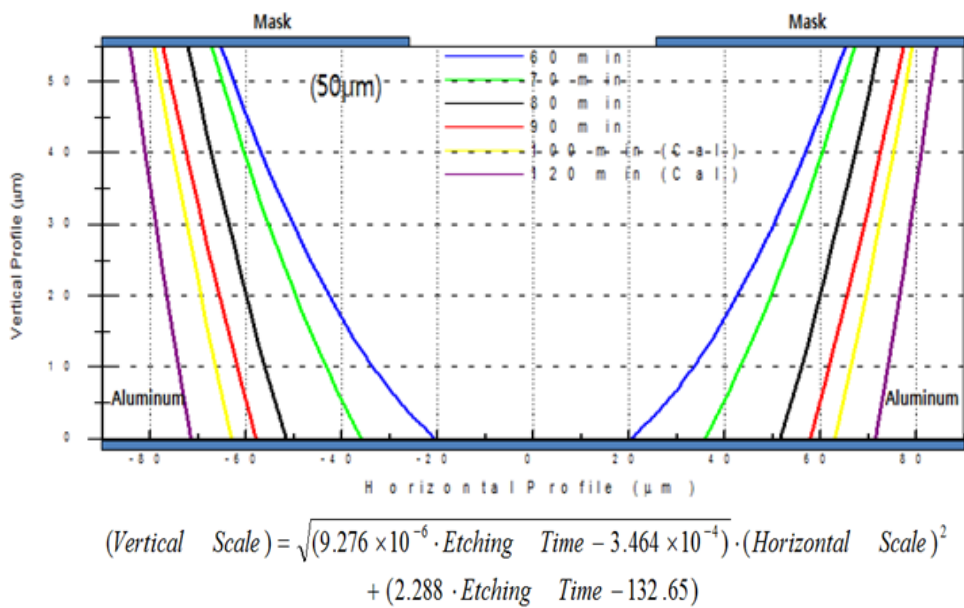$$+ (2.288 \cdot Etching \quad Time - 132.65)$$

Figure 3.6 Experimentally fitted cross-sectional cavity wall geometry with aluminum thickness of 55 µm with window opening size of 50 µm.

16

The maximum achievable aspect ratio from this fabrication method is measured to be ~1.1, and the cavity characteristic dimension can be reduced even further if the foil thickness is reduced proportionately. The foil thickness can be controlled with an accuracy of ±3 µm with the Al_2O_3 growth process. An SEM image of a fabricated cavity with top and bottom diameters of 150/100 µm (±2 µm) is presented in Figure 3.7. Additionally, the parameters which can be controlled are the cavity diameters (L_1 and L_2), the opening angle of the parabolic wall (Θ), and the thickness of the foil (L_3). The capability of controlling the cavity wall geometry is useful in studying plasma characteristics as the properties of the plasma can be changed due to a different electric field distribution in the cavities.
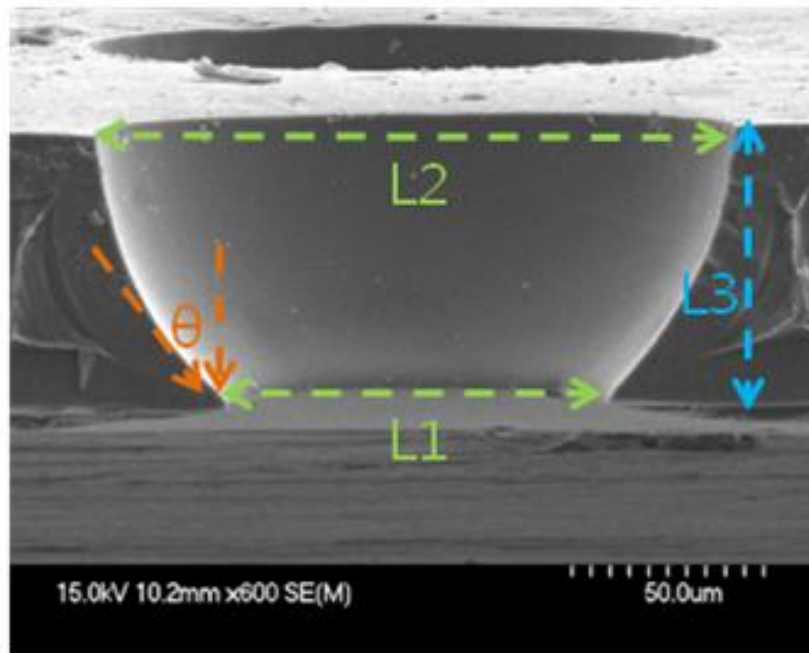

Figure 3.7 SEM image of an Al/Al_2O_3 cavity with a parabolic cross section and a buried aluminum electrode. Cross-sectional view of cavity with an upper diameter of 150 µm and a bottom diameter of 100 µm. The diameters of the cavities, the thickness of electrode, and the opening aperture angle can be controlled.

Controlling the geometry is especially important in the field of fluid dynamics. A parabolic wall geometry has proven to be effective for applications which require high Reynold's number (>1500). For example, a new application of microplasmas using the parabolic cross-sectional Al/Al_2O_3 devices has resulted in developing microdischarge thrusters (MCDT) for adjusting the primary and secondary orbits of small satellites [11]. This work has been conducted in collaboration with the Electric Propulsion Laboratory of the Department of Aerospace Engineering at the University of Illinois at Urbana-Champaign.

CHAPTER 4

EXPERIMENTAL RESULTS

4.1 Motivation

The effective discharge gap is well defined for the case of DC parallel plates and microhollow cathode devices, as described in Chapter 2. However, in the case of the Al/Al_2O_3 devices presented in Figure 2.5, the effective distance of the structure has not yet been determined. As the general goal in the future is to continue decreasing the cavity diameter dimensions below a Debye length (~5 µm), it is essential to understand how the devices will behave as the cavity dimension decreases below ~50 µm. In short, the goal of this chapter is to present the results of a series of measurements in which the inter-electrode gap and the cavity diameter have both been varied systematically.

This experimental result will help understand ignition voltage behavior and will be referenced when designing future smaller characteristic dimension devices. In addition, this step is also essential to considering the electrochemical etching process used when fabricating cavity arrays. Since the cavity diameter is a function of aluminum foil thickness (with the highest aspect ratio of ~1.1), reducing the foil thickness is unavoidable as the cavity diameter becomes smaller than ~50 µm. Therefore, it was necessary to study the effect of reducing the aluminum foil.

4.2 Experimental Setup

Instead of using the previously proposed device geometry in Figure 2.5, the cavity-to-foil overlapped geometry shown in the Figure 4.1 is used for simplicity. The cavity diameter (D_1), aluminum electrode thickness (d_2), vertical and horizontal oxide thicknesses (d_3, d_4), and total

electrode thickness (d_5) are controlled by the combination of anodization and electrochemical etching processes with a precision of ±3 µm. The flat electrode thickness is kept at a constant aluminum thickness of 130 µm for all devices. Cavities are fabricated as described in Chapter 3, with etching duration of 120 min, which results in a slightly linear sidewall geometry with the top and bottom diameter differences of less than ± 5 µm.

Three different parameters – cavity diameter (D_1), aluminum electrode thickness (d_2), and vertical and horizontal oxide thicknesses (d_3 and d_4) – are individually varied one at a time when all other parameters are held constant. The cavity diameters are varied from 100 µm to 225 µm, aluminum thicknesses from 65 µm to 100 µm, and aluminum oxide thickness from 10 µm to 15 µm; the influence of each parameter on device behavior has been systematically studied.

Parameters:
D_1: Cavity Diameter
d_2: Aluminum Thickness
d_3: Vertical Al_2O_3 thickness
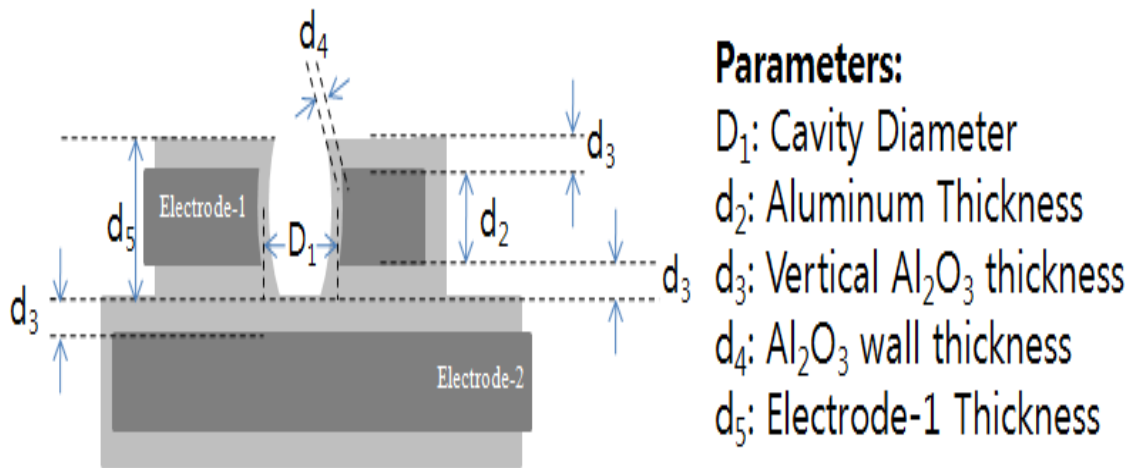d_4: Al_2O_3 wall thickness
d_5: Electrode-1 Thickness

Figure 4.1 Cross-sectional schematic of the Al/Al_2O_3 cavity-to-foil structured device employed in these studies.

Fabricated devices are evacuated to $<10^{-6}$ Torr and back-filled with research grade Ne gas to pressures ranging from 400 Torr to 1100 Torr. The high pressure limit is set by the pressure gauge. The lower pressure limit is the result of the 550 V_{pp} maximum voltage that can be

generated from a custom circuit which produces a 100 kHz bipolar signal with a duty cycle and a rise time of 40% and 0.3 µs, respectively. Ne gas is selected for its relatively low ignition voltage as well as its bright orange color which simplifies detection. The ignition of the plasma was identified by using a photodiode with a response time of tens of nanoseconds. Previously acquired photodiode response time data for Al/Al_2O_3 devices indicates that the plasma is ignited 0.32~0.35 µs after the threshold voltage is applied. Therefore, it can be assumed that the ignition voltage is detected instantaneously when observing the photodiode data.

4.3 Results

In Sections 4.3.1 to 4.3.3, the series of measurements of the device ignition voltages are presented when the three parameters – cavity diameter, aluminum (electrode) thickness, and the inter-electrode distance – are varied one at a time with the cavity-to-foil device structure shown in Figure 4.1.

4.3.1 Cavity diameter dependence

The variation of the ignition voltage with the cavity diameter (D_1) and various operating pressures has been investigated. The cavity diameter is varied from 100 µm to 225 µm with 65 µm of fixed aluminum foil thickness, and 10 µm of both vertical and horizontal aluminum oxide thicknesses. The operating pressure was varied from 400 to 1100 Torr. The resulting measurements are presented in Figure 4.2. On the left side of Figure 4.2, the ignition voltage is plotted as a function of the product of the gas pressure (p) and the cavity diameter (D_1) ranging from 4 ~ 27 Torr·cm. However, it should be noted that the minimum ignition voltages for each device with different cavity diameters occur at pD_1 values of 10, 13.65, 16, 19, and 22.5 Torr·cm. This range of values is not reasonable when compared with the Paschen's law presented in

Figure 2.4, and the pD_1 values do not follow Paschen's law. This can be confirmed from the right-hand plot of Figure 4.2, which shows the ignition voltage as a function of measured gas pressures from 400 Torr to 1100 Torr. To avoid the confusion of including all five curves, only the minimum and the maximum cavity diameters – 100 µm and 225 µm, respectively – are plotted. If the cavity diameter were to be the effective distance influencing Paschen's law, then the optimal pressure which gives the lowest ignition voltage of ~270 V_{pp} must be changed as the cavity diameters are varied at 1000 Torr. The graphs nearly overlap each other and they lie within the error bars. Therefore, the cavity diameter is not the dimension to be used for Paschen's law.
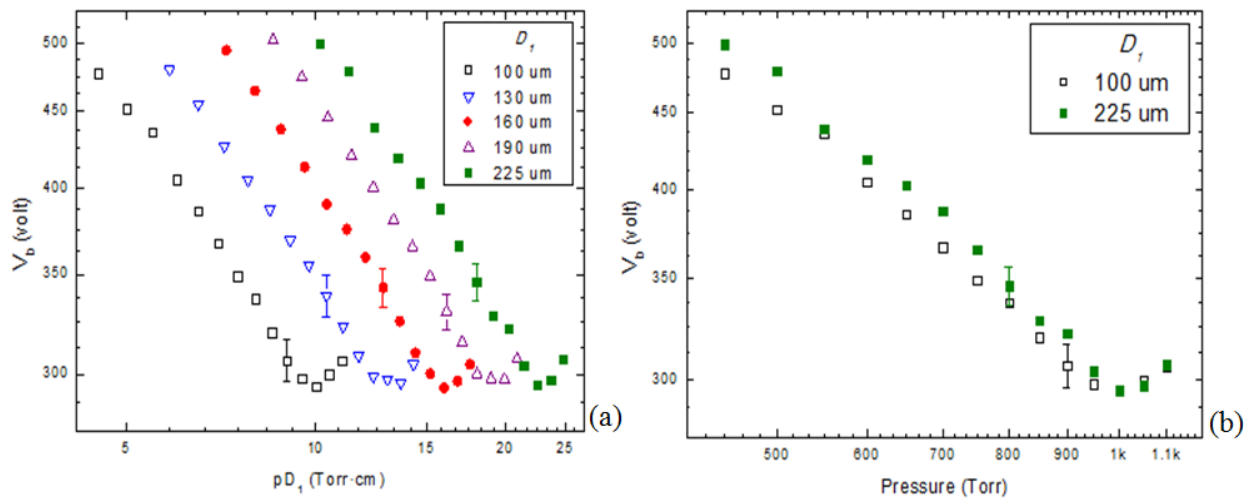

Figure 4.2 (a) Ignition voltage plot as a function of pD_1. Cavity diameters (D_1) of 100, 130, 160, and 190 µm are tested. (b) Ignition voltage plot as a function of operating pressures from 400 Torr to 1100 Torr. The cavity diameters of 100 µm and 225 µm are plotted.

4.3.2 Electrode thickness dependence

The variation of ignition voltage with the electrode thickness (d_2) and various operating pressures has been investigated. The electrode thickness, d_2, is varied from 65 µm to 100 µm with 225 µm of fixed cavity diameter and 10 µm aluminum oxide thicknesses. The operating

22

pressure was varied from 400 Torr to 1100 Torr. The resulting plots are presented in Figure 4.3, where the left plot represents the ignition voltage as a function of the product of the gas pressure and the thickness of the electrode (d_2).
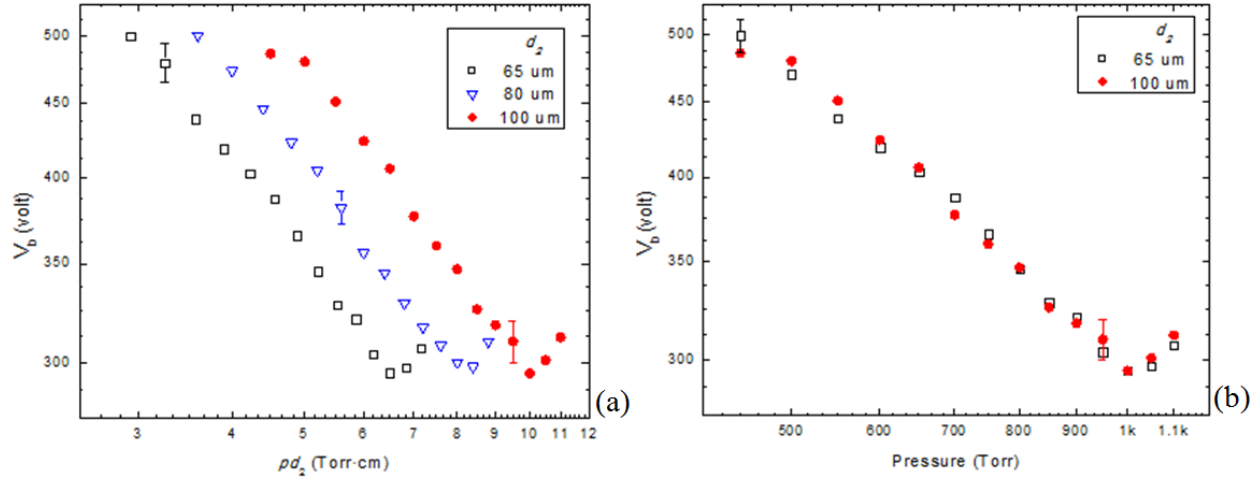

Figure 4.3 (a) The ignition voltage plot as a function of pd_2. The electrode thicknesses (d_2) of 65, 80, and 100 µm are tested. (b) The ignition voltage plot as a function of the operating pressures of 400 Torr to 1100 Torr. The electrode thicknesses of 65 µm and 100 µm are plotted.

The optimal pd_2 values which give the lowest ignition voltage from each device are measured to be 6.5, 8.4, and 10 Torr·cm. These values are slightly higher than the expected range of pd values, and as the thickness of aluminum is varied, shifts of the optimal pd_2 values have been observed. However, the right-hand plot of the Figure 4.3 implies that this aluminum thickness (d_2) does not influence Paschen's law. The right-hand plot of Figure 4.3 shows the ignition voltage as a function of the operating pressure. Similar to the cavity dependence plot, only the maximum and minimum values of the aluminum thickness have been presented to avoid confusion due to closely packed data points. The plots again lie very close to each other within the range of the error bars, and no shift of the optimal operating pressure has been observed. Therefore, it can be said that the aluminum electrode distance (d_2) is also not the correct dimension to insert into Paschen's law.

4.3.3 Inter-electrode distance dependence

The ignition dependence on the inter-electrode distance and various operating pressures has been investigated. The aluminum oxide thicknesses (d_3) for both the top and bottom electrode are varied from 10 µm to 15 µm with fixed aluminum thickness of 65 µm and 130 µm for both the cavity-electrode and foil-electrode gaps. The cavity diameter (D_1) is fixed at 225 µm while the operating pressure is varied from 400 Torr to 1100 Torr. The resulting plots are presented in Figure 4.4. The left-hand plot shows the ignition voltage as a function of the product of the gas pressure (p) and the inter-electrode distance ($2d_3$). The optimal values of p_2*d_3 for each device were measured to be 2 and 2.85 Torr·cm, respectively. This range of pd values is slightly lower than the calculated pd values for neon, but, interestingly, the shift of the optimal pressure which provides the lowest ignition voltage has been observed from the right-hand plot of Figure 4.4.
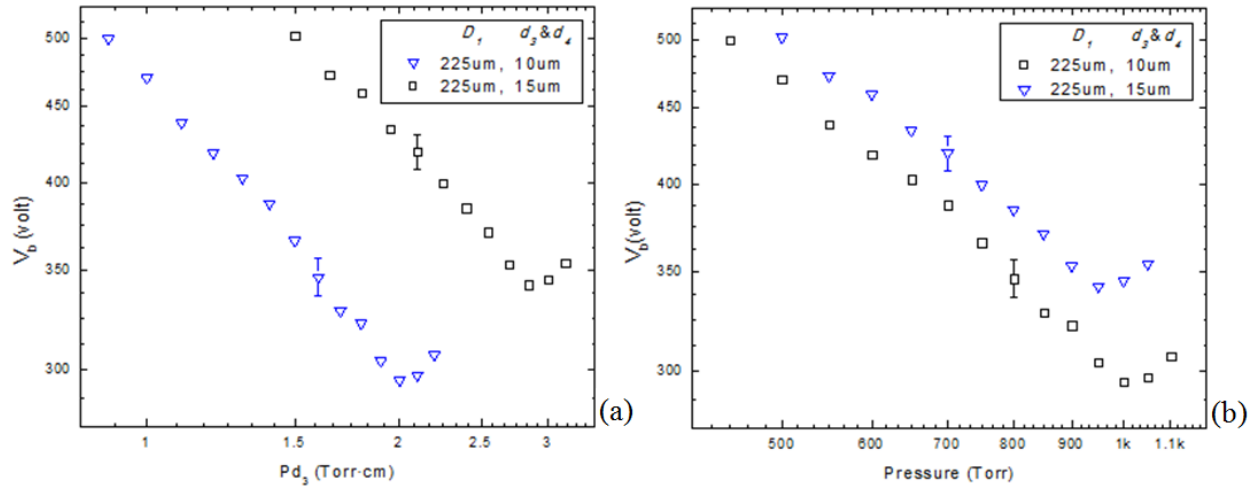
Figure 4.4 (a) Ignition voltage plot as a function of pd_3. Inter-electrode gaps (d_3) of 10 and 15 µm are tested. (b) Ignition voltage plot as a function of operating pressures of 400 Torr to 1100 Torr. Inter-electrode-gaps of 10 µm and 15 µm are plotted.

This plot provides the ignition voltage as a function of operating pressure, and the ~50 Torr difference between optimal pressures for the lowest ignition voltages indicates that the effective

24

distance for Paschen's law has been changed while differentiating the inter-electrode gap by growing thicker Al_2O_3 layers onto aluminum electrodes. Even though the measured values of pd_3 fall into a slightly lower range of the predicted values, the shift of the right-hand plot of Figure 4.4 indicates that modifying the inter-electrode gap must be more appropriate for the Paschen's law.

4.4 Conclusion

In conclusion, Al/Al_2O_3 microplasma devices with cavity-to-foil structure have been fabricated by sequences of wet electrochemical processes. The cavity diameters, electrode thickness, and inter-electrode gap have been systematically varied to investigate whether the Al_2O_3 devices obey Paschen's law. The experimental results show that cavity diameter and electrode thickness of 65~225 µm and 65~100 µm, respectively, do not satisfy the Paschen's law due to absence of optimal operating pressure differences when each parameter is varied. When changing the inter-electrode distance from 20 µm to 30 µm, however, ~50 Torr of optimal operating pressure has been observed and the resulting minimum pd values ranged from 2~2.85 Torr·cm. The minimum pd values are off by a factor of approximately two compared to the Paschen curve presented in Figure 2.4, but it is evident that the inter-electrode gap is appropriate for Paschen's law. Further studies with a wider range of inter-electrode distances, pressures, and applied voltages will be performed in the future.

REFERENCES

[1] J. W. Frame, D. J. Wheeler, T. A. DeTemple, and J. G. Eden, "Microdischarge devices fabricated in silicon," *Appl. Phys. Lett.*, vol. 71, no. 9, p. 1165, 1997.

[2] J. G. Eden, S.-J. Park, N. P. Ostrom, S. T. McCain, C. J. Wagner, B. A. Vojak, J. Chen, C. Liu, P. von Allmen, F. Zenhausern, D. J. Sadler, C. Jensen, D. L. Wilxoc, and J. J. Ewing, "Microplasma devices fabricated in silicon, ceramic, and metal/polymer structures: Arrays, emitters and photodetectors," *J. Phys. D: Appl. Phys.*, vol. 36, p. 2869, 2003.

[3] S.-J. Park and J. G. Eden, "Microdischarge devices with a nanoporous Al_2O_3 dielectric: Operation in Ne and air," *IEEE Trans. Plasma Sci.*, vol. 33, no. 2, p. 572, 2005.

[4] D. Yarmolich, Ya. E. Krasik, E. Stambulchik, V. Bernshtam, J. K. Yoon, B. Herrera, S.-J. Park, and J. G. Eden, "Self-pulsing, 10^4 A-cm^{-2} current density discharges in dielectric barrier Al/Al_2O_3 microplasma devices," *Appl. Phys. Lett.*, 94, no. 1, p. 11501, 2009.

[5] S.-J. Park, K. S. Kim, and J. G. Eden, "UV generation in microcavity plasma devices with encapsulated Al_2O_3/Al electrodes," in *32nd IEEE International Conference on Plasma Science*, 2005, p. 168.

[6] S.-J. Park, K. S. Kim, and J. G. Eden, "Ultraviolet emission intensity, visible luminance, and electrical characteristics of small arrays of Al/Al_2O_3 microcavity plasma devices operating in Ar/N_2 or Ne at high-power loadings," *J. Appl. Phys.*, vol. 99, no. 2, p. 26107, 2006.

[7] J. G. Eden, S.-J. Park, and K. S. Kim, "Arrays of nonequilibrium plasmas confined to microcavities: An emerging frontier in plasma science and its applications," *Plasma Sources Sci. and Tech.*, vol. 15, no. 2, pp. S67-S74, 2006.

[8] S.-J. Park, J. D. Readle, A. J. Price, J. K. Yoon, and J. G. Eden, "Lighting from thin (<1 mm) sheets of microcavity plasma arrays fabricated in Al/Al_2O_3/glass structures: Planar, mercury-free lamps with radiating areas beyond 200 cm^2," *J. Phys. D: Appl. Phys.*, vol. 40, no. 13, p. 3907-3913, 2007.

[9] S.-J. Park, K. S. Kim, A. J. Price, P. A. Tchertchian, P.-Y, Chen, J. K. Yoon and J. G. Eden, "Large scale arrays of microcavity plasma devices based on encapsulated Al/Al_2O_3 electrodes: Device characteristics as a plasma display pixel and low cost wet chemical fabrication processing," *Digest of Tech. Papers - SID Int. Sym.*, vol. 38, no. 1, p. 538, 2007.

[10] J. D. Readle, K. E. Tobin, K. S. Kim, J. K. Yoon, J. Zheng, S. K. Lee, S.–J. Park, and J. G. Eden, "Flexible, lightweight arrays of microcavity plasma devices: Control of cavity geometry in thin substrates," *IEEE Trans. Plasma Sci.*, vol. 37, no. 6, p. 1045, 2009.

[11] R. L. Burton, J. G. Eden, S.-J. Park, J. K. Yoon, M. Chadenedes, S. Garrett, J. L. Woodard, G. Benavides, and D. Carroll, "Initial development of the microcavity discharge microthruster," in *31st International Electric Propulsion Conference*, 2009.

[12] K. S. Kim, J. K. Yoon, S.-J. Park, and J. G. Eden, "Intense green luminescence from 20,000 pixel arrays of Al/Al$_2$O$_3$ microcplasma devices with parabolic cross-sectional cavities," *IEEE Trans. Plasma Sci.*, vol. 36, no. 4, part 1, p. 1258, 2008.

[13] K. S. Kim, J. K. Yoon, E. Xie, T.-L. Kim, G. Heimberg, S.-J. Park, and J. G. Eden, "Fully addressable, self-assembled microcavity plasma array: Improved luminous efficacy by controlling device geometry," *Digest of Tech. Papers – SID Int. Symposium*, vol. 39, no. 1, p. 382, 2008.

[14] K. S. Kim, T. L. Kim, J. K. Yoon, S.-J. Park, and J. G. Eden, "Control of cavity cross-section in microplasma devices: Luminance and temporal response of 200 x 100 and 320 x 160 arrays with parabolic Al$_2$O$_3$ microcavities," *Appl. Phys. Lett.*, vol. 94, no. 1, p. 011503, 2009.

[15] A. Fridman and L. A. Kennedy, *Plasma Physics and Engineering*. New York, NY: Taylor & Francis, 2004.

[16] M. Moselhy, I. Petzenhauser, K. Frank, and K. H. Schoenbach, "Excimer emission from microhollow cathode argon discharges," *J. Appl. Phys. D*, vol. 36, no. 23, p. 2922, 2003.

[17] K. Tachibana, "Design and control of microplasma devices based on spectroscopic diagnostics," in *2nd International Workshop on Microplasmas*, 2004.

[18] Y. P. Raizer, *Gas Discharge Physics*. Berlin, Germany: Springer Verlag, 1991.

[19] K. H. Becker, K. H Schoenbach, and J. G. Eden, "Microplasmas and applications," *J. Phys. D: Appl. Phys.*, vol. 39, no. 3, pp. R55-R70, 2006.

[20] J. W. Diggle, T. C. Downie, and C. W. Coulding, "Anodic oxide films on aluminum," *Chem. Rev.*, vol. 69, no. 1, p. 365, 1969.

[21] G. E. Thompson, Y. Xu, P. Skeldon, K. Shimizu, S. H. Han, and G. C. Wood, "Anodic oxidation of aluminum," *Philosophical Mag. B*, vol. 55, no. 6, p. 651, 1987.

[22] G. C. Wood, P. Skeldon, G. E. Thompson, and K. Shimizu, "A model for the incorporation of electrolyte species into anodic alumina," *J. Electrochemical Soc.*, vol. 143, no. 1, p. 74, 1996.

[23] K. Shimizu, K. Kobayashi, G. E. Thompson, and G. C. Wood, "A novel marker for the determination of transport numbers during anodic barrier oxide growth on aluminum," *Philosophical Mag. B*, vol. 64, no. 3, p. 345, 1991.

[24] G. Thompson and G. C. Wood, "Anodic films on aluminum," in *Treatise on Materials Science and Technology*, vol. 23. New York, NY: Academic Press, 1983, pp. 205-329.

[24] S. Shingubara, "Fabrication of nanomaterials using porous alumina templates," J. Nanoparticle Research, vol. 5, no. 1-2, p. 17, 2003.

[26] R. B. Wehrspohn and J. Schilling, "Electrochemically prepared pore arrays for photonic crystal applications," *Mat. Research Soc. Bulletin*, vol. 26, no. 8, p. 623, 2001.

[27] G. Sauer, G. Brehm, S. Schneider, K. Nielsch, R. B. Wehrspohn, J. Chio, H. Hofmeister, and U. Gösele, "Highly ordered monocrystalline silver nanowire arrays," *J. Appl. Phys.*, vol. 2, no. 5, p. 3243, 2002.

[28] X. Zhao, P. Jiang, S. Xie, L. Liu, W. Zhou, Y. Gao, L. Song, J. Wang, D. Liu, X. Dou, S. Luo, Z. Zhang, Y. Xiang, and G. Wang, "Anodizing behavior of aluminum foil patterned with SiO2 mask," *J. Electrochemical Soc.*, vol. 152, no. 10, pp. B411-B414, 2005.

[29] J. R. Dickey, J. L. Davidson, and Y. Tzeng, "Improved dielectric properties for anodic aluminum oxide films by soft/hard two-step electrolytic anodization," *J. Electrochemical Soc.*, vol. 136, no. 6, p. 1772, 1989.

[30] S.-J. Park, K. S. Kim, and J. G. Eden, "Nanoporous alumina as a dielectric for microcavity plasma devices: Multilayer Al/Al_2O_3 structures," *Appl. Phys. Lett.,* vol. 86, no. 22, p. 221501, 2005.